molecules

MDPI

Article

Machine Learning-Assisted DFT Screening of Nitrogen-Doped Graphene Diatomic Catalysts for Nitrogen Reduction Reaction

Xiulin Wang [1,2], Suofu Nie [1,2], Huichao Yao [1,2], Sida Wu [1,2], Yanze Li [3], Junli Feng [3], Yiyan Sui [1,2], Yuqing Zhang [1,2], Xinwei Wang [3] and Xiuxia Zhang [3,*]

1 CNOOC Key Laboratory of Liquefied Natural Gas and Low-Carbon Technology, Beijing 100028, China
2 CNOOC Gas & Power Group, Research & Development Center, Beijing 100028, China
3 Department of Energy and Power Engineering, College of New Energy, China University of Petroleum (East China), Qingdao 266580, China
* Correspondence: zhangxx@upc.edu.cn

Abstract

This research seeks to investigate extremely efficient catalysts for the nitrogen reduction process (NRR), utilizing machine learning (ML)-aided density functional theory (DFT) computations. Specifically, we investigate dual transition metal atoms anchored on hexagonal nitrogen-doped graphene (TM_1-TM_2@N_6G) as prospective high-activity catalysts for the NRR. The findings indicate that the synergistic effect of dual transition metal atoms in the TM_1-TM_2@N_6G catalyst overcomes the intrinsic constraints of the linear relationship among intermediates, facilitating the activation and adsorption of N_2, thereby exhibiting significant potential for ammonia synthesis through N_2 reduction. Particularly, four catalysts screened by ML and DFT exhibit good stability and excellent selectivity and activation towards N_2. Among them, the catalysts Ti-Cr@N_6G, Ti-Mo@N_6G, and Ti-Pd@N_6G possess two reaction pathways with minimum reaction energies of 0.55 eV, 0.50 eV, and 0.40 eV, respectively. Remarkably, Ti-Co@N_6G, which features a single reaction pathway, exhibits a reaction energy lower than 0.05 eV, allowing the NRR to proceed spontaneously. It is noteworthy that incorporating ML into DFT calculations facilitates the rapid screening of all transition metal combinations, significantly accelerating the research on catalytic performance and optimizing the selection of catalysts.

Keywords: dual-atom catalysts; machine learning screening; nitrogen-doped graphene; nitrogen reduction reaction; density functional theory calculation

check for updates

Academic Editors: M. Natália D.S. Cordeiro and Albin Pintar

Received: 11 August 2025
Revised: 13 September 2025
Accepted: 21 September 2025
Published: 20 October 2025

Citation: Wang, X.; Nie, S.; Yao, H.; Wu, S.; Li, Y.; Feng, J.; Sui, Y.; Zhang, Y.; Wang, X.; Zhang, X. Machine Learning-Assisted DFT Screening of Nitrogen-Doped Graphene Diatomic Catalysts for Nitrogen Reduction Reaction. *Molecules* **2025**, *30*, 4131. https://doi.org/10.3390/molecules30204131

Copyright: © 2025 by the authors. Licensee MDPI, Basel, Switzerland. This article is an open access article distributed under the terms and conditions of the Creative Commons Attribution (CC BY) license (https://creativecommons.org/licenses/by/4.0/).

1. Introduction

Ammonia, as an important inorganic chemical product and raw material, plays a pivotal role in the production of nitrogen fertilizers and nylon and holds potential for hydrogen storage [1] and zero-carbon energy sources [2]. However, the primary method for ammonia synthesis in industry is the Haber–Bosch process ($N_2(g) + 3H_2(g) \rightarrow 2NH_3(g)$), which activates inert N_2 (with a molecular bond energy of 945 kJ/mol) and converts it to NH_3 with the aid of iron or ruthenium-based catalysts under high-temperature and high-pressure conditions (350–550 °C, 150–350 atm) [3,4]. This process is plagued by issues such as high energy consumption, significant CO_2 emissions, and low conversion rates, failing to meet the demands for environmental protection and green catalysis in the context of the "dual carbon" strategy. Furthermore, the harsh production conditions result in the extensive use of fossil fuels, which also adversely affects the environment [5]. Although

the nitrogen source in NRR technology is readily available, the hydrogenation reaction is difficult to achieve due to the chemical inertness of the N≡N bond, significantly reducing the catalytic reaction rate and imposing stringent requirements on reaction conditions. Therefore, there is an urgent need to develop a highly active novel catalyst that can achieve ammonia synthesis under low-temperature and low-pressure conditions, thereby reducing costs and technical difficulties.

In the past decade, the emergence of atomic-scale catalysts has injected new vitality into the field of catalysis. These special supported metal catalysts (SACs) boast high atom utilization, high catalytic activity, controllable selectivity, and good stability, garnering increasing attention [6–10]. Numerous experiments and studies have demonstrated that isolated single atoms, particularly transition metal atoms embedded or anchored on suitable substrates, can effectively catalyze NRR [11–14]. However, due to the existence of isolated active centers, it is difficult to carry out multi-atom synergistic catalysis [15]. To further enhance atom utilization and consider the impact of different atom combinations on the catalytic process, researchers have focused on introducing new metal atoms into SACs to create dual-atom catalysts (DACs). It has been found that these catalysts not only improve the loading rate of metal atoms and functional active sites but also achieve efficient atom utilization. The two metal atoms can cooperate to effectively tune their d-band centers, enhancing the interaction between reactants or intermediates and catalytically active sites [16–18]. However, the diversity of combinations for such dimetallic active sites significantly increases the workload in the search for highly active NRR metal diatomic catalysts.

In recent years, with the rapid advancement of machine learning methods, the speed and efficiency of theoretical catalyst screening are expected to see significant improvements. Traditional empirical models are often constrained by limited chemical intuition and trial-and-error approaches, leading to inefficient catalyst development and lengthy cycles [19]. In contrast, machine learning technology can accelerate the discovery and optimization of new catalytic materials by swiftly identifying potential high-activity catalyst structures and guiding experimental design through big data analysis and model predictions. This innovation not only helps reduce costs but also drives progress in catalytic science and industry for key reactions such as ammonia synthesis, providing crucial support for sustainable development. Consequently, a growing number of studies have recently explored the use of machine learning (ML) methods for catalyst discovery and design [20–24]. Machine learning typically relies on data-driven models that utilize regression or classification algorithms for training on existing datasets. Once trained, these models can predict the target variable, or desired outcome, based on the key features of the input. Therefore, machine learning serves as a powerful tool for researchers to quickly screen potential catalyst candidates within the vast chemical space. By analyzing extensive chemical data and physical properties, these algorithms can identify catalyst structures with high activity and selectivity, thereby expediting the new material development process. This approach not only enhances the efficiency of catalyst design but also offers valuable guidance and optimization directions for laboratory research [25,26]. Compared to traditional theoretical calculations like density functional theory (DFT), ML-assisted DFT can significantly reduce computational costs, better comprehend the potential relationship between material structure and catalytic performance, and effectively identify intrinsic catalyst descriptors [16–18,26–33]. Therefore, when combined with ML-assisted DFT calculations, the design and optimization of NRR diatomic catalysts can be effectively explored, particularly in the rapid screening of candidates, showcasing broad prospects.

In this study, we selected 18 different combinations of transition metal atoms to serve as active sites in the DAC model. By cross-combining these atoms, we designed a total of 171 catalysts with the objective of thoroughly exploring their catalytic potential. We then

chose 6-nitrogen-doped graphene (N_6G) as the substrate and abbreviated these diatomic catalysts as TM_1-TM_2@N_6G. The structural and performance parameters of the catalysts were derived from a chemical property database and simple DFT calculations, which were used to assess the performance of 25 groups of TM_1-TM_2@N_6G catalysts. For machine learning screening, we employed four indicators: catalyst binding energy, adsorption energy of N_2 on the catalyst, the energy of the first hydrogenation step, and ammonia dissociation energy. We utilized three machine learning algorithms for comparative screening: the random forest algorithm, k-nearest neighbor regression, and a decision tree. Ultimately, we successfully screened four TM_1-TM_2@N_6G catalysts that demonstrated high activity and selectivity during N_2 activation. The stability of these catalysts, as well as the extent of N_2 activation and the reaction energy barrier, were evaluated using ab initio molecular dynamics (AIMD), Bader charge analysis, projected density of states (PDOS), and energy band analysis. The results indicate that the double-transition metal atoms anchored to the N_6G monolayer can effectively reduce N_2 to NH_3, showcasing their broad application potential in nitrogen reduction reactions.

2. Structure and Discussion

2.1. TM_1-TM_2@N_6G Catalyst Structure and Stability

Previous studies have extensively explored the characteristics and performance of nitrogen-doped graphene (NG) as a catalyst substrate [34]. NG is renowned for its excellent stability, maintaining superior catalytic performance under harsh conditions [35]. Furthermore, NG features tunable active site coordination structures [36,37]. According to prior research, hexa-nitrogen coordination structures have been found to be beneficial for dual-Atom catalysts (DACs) by facilitating direct charge transfer between two metal atoms connected via a metal–metal bond. Additionally, tri-nitrogen coordination structures have demonstrated exceptional electron transfer properties and catalytic activity in DACs [35,38]. Therefore, this study focuses on investigating the micro-coordination structure (N_6G), wherein a single metal atom is coordinated by three nitrogen atoms.

In the selection of metal atoms, those from the 3d, 4d, and 5d transition series, as well as main group metals, exhibit promising potential as active sites in catalysts. Thus, we chose 18 transition metal atoms for the TM_1-TM_2@N_6G model, as illustrated in Figure 1a. To succinctly describe the catalysts' structure and type, a series of dual-atom catalysts (DACs) is denoted as TM_1-TM_2@N_6G, as shown in Figure 1b. Here, TM1 and TM2 represent transition metal atoms anchored on the N_6G surface, including Ti, V, Cr, Mn, Fe, Co, Ni, Cu, Zn, Zr, Nb, Mo, Ru, Rh, Pd, Ag, Cd, and Au. Considering the structural diversity and complexity of TM_1-TM_2@N_6G, these 18 metal atom combinations yield a total of 171 possible TM_1-TM_2@N_6G catalysts. However, conducting DFT calculations for all 171 catalysts would be computationally intensive and time-consuming, resulting in inefficient use of resources. Therefore, we randomly selected 25 catalysts for performance exploration, serving as the dataset for subsequent machine learning (ML) screening.

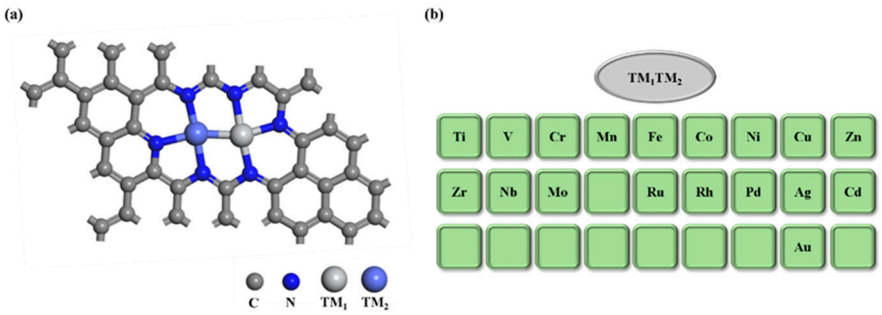


Figure 1. (**a**) Structure of TM_1-TM_2@N_6G. (**b**) The transition metal elements selected for this study.

The achievement of catalytic performance hinges on the structural stability of the catalyst. Only when the catalyst structure is stable can it effectively promote chemical reactions, thereby attaining the desired catalytic activity and selectivity. For the selected 25 TM_1-TM_2@N_6G structures, after structural optimization calculations, their formation energies (E_G) were computed using the formation energy formula, as depicted in Figure 2. A negative formation energy indicates that these structures are thermodynamically stable, as they can form spontaneously without requiring external energy. Conversely, a positive formation energy value indicates that these structures require additional external energy to form, rendering them thermodynamically unstable. Through an in-depth exploration of the structural properties of TM_1-TM_2@N_6G catalysts, significant differences have been identified. As illustrated in Figure 2, the 21 groups of catalysts exhibit robust stability, primarily attributed to their negative formation energies. Notably, the Au-Rh@N_6G and Mn-Zr@N_6G catalysts demonstrate exceptionally high binding energies of −2.87 eV and −2.84 eV, respectively, further highlighting their stability advantages. Four groups of catalysts display weaker stability, with formation energies approaching or even reaching positive values. Among these, the Mo-Mo@N_6G and Mo-Ru@N_6G catalysts, although their metal atoms remain bonded to the N_6G substrate without complete detachment, possess certain research potential. However, their positive binding energies indicate a relatively weaker stability. In contrast, the Ag-Ag@N_6G and Ag-Au@N_6G catalysts not only exhibit positive formation energies but also show evident structural instability, as their metal atoms have detached from the N_6G substrate. Consequently, they are unsuitable for subsequent research as stable catalysts. In summary, it can be concluded that the synthesis of stable TM_1-TM_2@N_6G catalysts is entirely feasible.

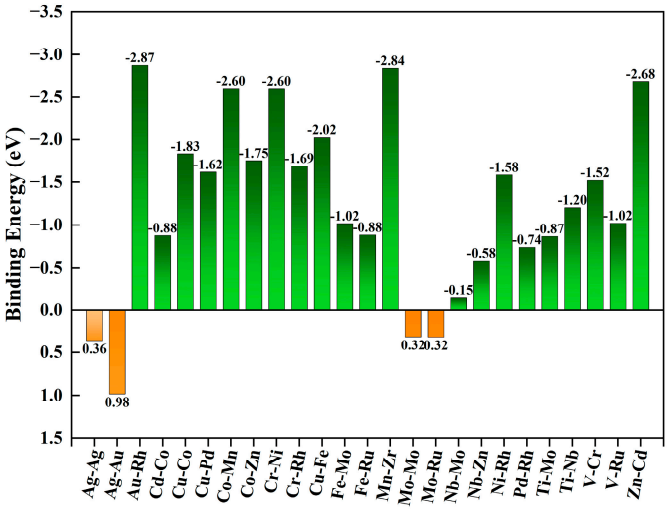


Figure 2. Binding energies of 25 TM_1-TM_2@N_6G.

2.2. Computational Screening of NRR Catalytic Candidates

The chemical reaction process of NRR is highly intricate, encompassing various potential reaction mechanisms such as distal, alternating, and enzymatic reactions (Figure 3a). Traditional research methodologies often involve utilizing density functional theory to comprehensively investigate all feasible reaction intermediates, aiming to pinpoint potential reaction pathways and theoretical rate-determining steps. However, this approach entails substantial computational expenses, rendering it particularly inefficient for large-scale catalyst screening endeavors. To strike a balance between computational cost and efficiency in catalyst screening, we have adopted a simplified approach: selecting specific descriptors to offer a brief description of the NRR reaction. These descriptors may encompass pivotal physical or chemical attributes, including electron affinity, atomic charge distribution, and

the stability of reaction intermediates, among others. By leveraging these descriptors, we can promptly assess the potential activity and selectivity of diverse catalysts in the NRR process, thereby strategically diminishing the pool of candidate catalysts necessitating detailed computations. This refined approach facilitates a more efficient evaluation of catalyst performance, optimizing the selection procedure for efficacious NRR catalysts.

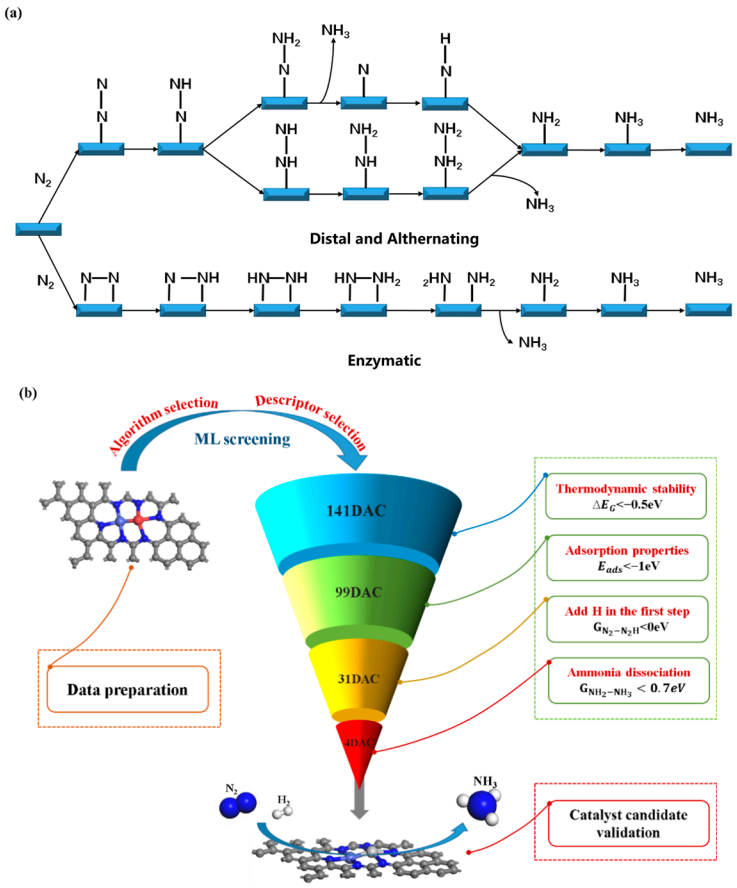


Figure 3. (**a**) The reaction mechanism of NRR and (**b**) the screening criteria of ΔE_G, E_{ads}, $\Delta G_{N_2-N_2H}$, $\Delta G_{NH_2-NH_3}$ and the ML screening process.

The structural stability of a catalyst is a fundamental prerequisite for its functionality. In the NRR process, if the TM_1-TM_2@N_6G catalyst lacks stability, it becomes irrelevant to the reaction. Therefore, we consider the catalyst binding energy (ΔE_G) as a crucial descriptor. Furthermore, when the TM_1-TM_2@N_6G catalyst participates in the NRR reaction, its chemisorption of N_2 is of utmost importance. Effective chemisorption can fully activate the inert N≡N triple bond, reducing the required reaction energy between the N≡N bonds, lowering the reaction barrier, and increasing the frequency of effective collisions between the reactant and the catalyst. Consequently, we consider the adsorption energy (E_{ads}) of N_2 as the second descriptor. Additionally, an examination of all reaction intermediates in the NRR process reveals that the initial step of adding H to form N_2H (N_2 + H = N_2H) and the final step of H desorption to form NH_3 (*NH_2 + H = *NH_3) are consistently present, regardless of the NRR reaction mechanism. In NRR, due to the inertia of the N≡N triple bond, the first H addition step requires a significant reaction energy ($\Delta G_{N_2-N_2H}$) to break this bond, which is theoretically likely to be the rate-determining step in NRR. Therefore, we regard it as the third descriptor, reflecting the reaction's difficulty. Ammonia dissociation is also critical in the NRR reaction. The nitrogen atom forms four orbitals through sp^3 hybridization, three of which are half-filled; thus, its hybridization method is sp^3. When N atoms adsorb H atoms to form NH_2, only one sp^3 hybrid orbital remains, making it prone to

adsorption on the catalyst surface to form a stable structure. As a result, the formation and desorption of $*NH_2$ to $*NH_3$ on the catalyst require substantial free energy [39]. However, DFT calculations of the selected 25 catalysts revealed that the direct transition from $*N_2$ to $*N_2H$ is rare; instead, it often occurs through a side path from $*NH_2$ to NH_3. Many catalysts exhibit better activity via this lateral pathway without undergoing the $*NH_2$ to $*NH_3$ process. Therefore, we choose the energy change of $*NH_2$-NH_3 ($\Delta G_{NH_2-NH_3}$) as the fourth descriptor. Numerous studies have confirmed that $\Delta G_{NH_2-NH_3}$ and $\Delta G_{NH_2-NH_3}$ generally have large positive values throughout the reduction process for most catalysts, regardless of the reaction mechanism [40,41]. Thus, using $\Delta G_{N_2-N_2H}$ and $\Delta G_{NH_2-NH_3}$ as activity descriptors can effectively reflect the catalyst's performance. By employing these four descriptors, the screening efficiency can be significantly enhanced without compromising screening accuracy.

Based on the aforementioned analysis, we devised a two-step screening process: in the initial phase, ΔE_G and E_{ads} served as the primary screening criteria to eliminate catalysts with insufficient stability and poor N_2 activation. In the subsequent phase, highly active catalysts were screened using $\Delta G_{N_2-N_2H}$ and $\Delta G_{NH_2-NH_3}$. To identify the optimal DACs, we established the following criteria for each descriptor (Figure 3b): (i) ΔE_G should be less than -0.5 eV, ensuring robust stability; (ii) E_{ads} should be less than -1 eV, corresponding to the degree of chemisorption and activation of N_2; (iii) $\Delta G_{N_2-N_2H}$ should not exceed 0 eV, ensuring that the cleavage of the N≡N triple bond during NRR is a spontaneous process, thus significantly reducing the reaction's complexity; (iv) $\Delta G_{NH_2-NH_3}$ should not surpass 0.70 eV, which, according to the Arrhenius equation, suggests that the produced NH_3 can be swiftly removed. Furthermore, these four descriptors can be tailored to suit the specific requirements of individual research endeavors.

Firstly, the structures and reaction intermediates of 25 TM_1-$TM_2@N_6G$ were investigated using the DFT calculation method, from which the four descriptor parameters—ΔE_G, E_{ads}, $\Delta G_{N_2-N_2H}$, and $\Delta G_{NH_2-NH_3}$—for each of the 25 TM_1-$TM_2@N_6G$ systems were obtained.

The calculated four descriptor parameters are presented in Table S1, where the adsorption energy is denoted by the maximum adsorption energy observed among the various adsorption structures. As illustrated in Figure 4, the graphene-based double-transition metal atom DACs exhibit outstanding performance in terms of E_{ads}, $\Delta G_{N_2-N_2H}$, and $\Delta G_{NH_2-NH_3}$. From Figure 4a, it is evident that the adsorption energy of N_2 on the catalyst is less than 0, with a maximum adsorption energy of -2.01 eV. This indicates that the graphene-based DACs possess strong N_2 adsorption capabilities, thereby establishing a foundation for subsequent N_2 activation. Figure 4b shows that in the first hydrogenation step, three catalyst groups, namely Ti-Mo, Ti-Nb, and V-Cr, exhibit negative energy changes, while 16 groups have energy changes of less than 0.8 eV. This further indicates that DACs effectively activate the N≡N bond, reducing its bond energy and resulting in a low energy barrier for the initial hydrogenation activation reaction, which facilitates the reaction under milder conditions. As illustrated in Figure 4c, during the NH_3 dissociation process, six out of the 21 catalyst groups exhibit spontaneous NH_3 desorption, suggesting that these DACs possess good dissociation ability.

These four descriptor parameters serve as the target values for training and testing the ML model. Subsequently, input features are selected, which are crucial for constructing the ML model and identifying the intrinsic correlations within the input data. The chosen model features should reflect the atomic and electronic properties of various TM atoms, considering their interaction with N_6G. To ensure the efficiency of the ML method, these features should be readily obtainable through simple DFT calculations or direct database queries. Based on the aforementioned principles, eight distinct physicochemical properties were selected to characterize the key intermediate reactions in the TM_1-$TM_2@N_6G$ catalytic

NRR process for the ML model. The electronic structure of TM metal atoms is described by metal negativity (p), electron affinity (EA), first ionization energy (IE), and d electron number (N_d). Additionally, considering the unique structure of TM_1-TM_2@N_6G and the interaction between TM atoms and N_6G, we included the sum of the van der Waals radii (R) of TM atoms, the atomic mass (M) of TM atoms, and the atomic radii of the two TM atoms. Ultimately, we compiled 23 input features, as presented in Table 1. It is important to note that high correlation between features can adversely affect the performance of the ML model. Therefore, we utilized the Pearson correlation coefficient matrix to assess the correlation between feature pairs, eliminating features with high correlation among the input features and retaining those that are highly correlated with the output descriptor. With the assistance of ML methods, the catalytic performance of all TM combinations can be rapidly determined, enabling the exploration of interaction modes with key intermediates and the screening of ideal catalysts.

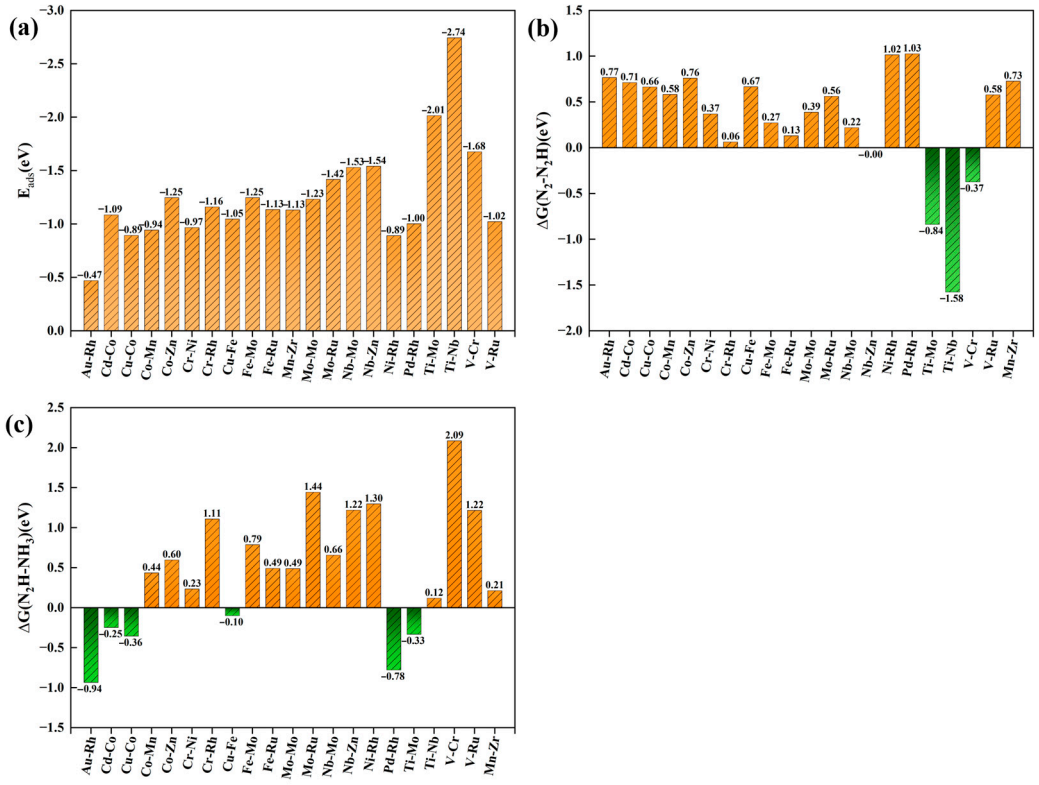


Figure 4. (**a**) E_{ads}, (**b**) $\Delta G_{N_2-N_2H}$, and (**c**) $\Delta G_{NH_2-NH_3}$ energy of 21 groups of DACs.

Based on the aforementioned conditions, we utilized three ML regression algorithms: RFR, KNR, and DT for ΔE_G, E_{ads}, $\Delta G_{N_2-N_2H}$, and $\Delta G_{NH_2-NH_3}$, respectively, to establish ML models for analysis. Each model was optimally tuned using a large number of parameters. We evaluated the models using R^2 and RMSE. To prevent overfitting during the tuning process, we included performance evaluations for both the training set and the test set. As shown in Table 2, the performance of the models based on the KNR and DT algorithms is significantly inferior to that of the RFR algorithm model. Therefore, we selected the RFR algorithm as the model algorithm for subsequent ML tasks.

Table 1. Machine learning initial input features.

Input Feature Value	Symbol	Input Feature Value	Symbol
The number of d orbital electrons of metal A	N_{dA}	The first ionization energy of metal B	IE_B
The number of d orbital electrons of metal B	N_{dB}	The absolute value of the first ionization energy between metals	IE
The absolute value of the number of d orbital electrons between metals	N_d	The electron affinity energy of metal A	EA_A
The sum of the number of d orbital electrons between metals	N_{dAB}	The electron affinity energy of metal B	EA_B
Electronegativity of metal A	p_A	The absolute value of the electron affinity between metals	E_A
Electronegativity of metal B	p_B	The atomic radius of metal A	R_A
The absolute value of the difference in electronegativity between metals	p_{A-B}	The atomic radius of metal B	R_B
The sum of electronegativity between metals	p_{A+B}	The sum of the atomic radii of the center of the metal	R_{A+B}
The number of s orbital electrons of metal A	N_{sA}	The atomic mass of metal A	M_A
The number of s orbital electrons of metal B	N_{sB}	The atomic mass of metal B	M_B
The absolute value of the number of s orbital electrons between metals	N_s	The atomic mass of metals A, B	M_{A+B}
The first ionization energy of metal A	IE_A		

Table 2. Comparison of three ML regression algorithms: RFR, KNR, and DT.

ML Algorithm	Evaluation Criterion	E_G/eV	E_{ads}/eV	$\Delta G_{N_2-N_2H}$/eV	$\Delta G_{NH_2-NH_3}$/eV
RFR	R^2	0.9054	0.9129	0.9233	0.9095
	RMSE	0.1698	0.1219	0.1664	0.1644
DT	R^2	0.8171	0.7071	0.6310	0.8417
	RMSE	0.4475	0.4613	0.5314	0.3739
KNR	R^2	0.7777	0.7655	0.6920	0.8164
	RMSE	0.3504	0.2134	0.3033	0.2752

The trained RFR model was used to predict the ΔE_G, E_{ads}, $\Delta G_{N_2-N_2H}$, and $\Delta G_{NH_2-NH_3}$ of the remaining 146 TM_1-TM_2@N_6G structures. The input dataset consisted of the atomic and electronic properties of 18 TM atoms, enabling us to efficiently screen highly active catalysts from 171 TM_1-TM_2@N_6G structures, thereby reducing computational costs. In this study, DFT calculations for ΔE_G, E_{ads}, $\Delta G_{N_2-N_2H}$, and $\Delta G_{NH_2-NH_3}$ for 25 TM_1-TM_2@N_6G structures alone took approximately 1200 h. In contrast, the training and prediction of the ML model, along with hundreds of tests of the three algorithms against four descriptors, were completed in less than 20 h. This demonstrates that the DFT-ML coupling approach used significantly reduces the computational cost. As a result, the research and screening efficiency for numerous catalysts has been improved.

Catalyst screening was conducted based on the descriptor parameters ΔE_G, E_{ads}, $\Delta G_{N_2-N_2H}$, and $\Delta G_{NH_2-NH_3}$ obtained from the ML model. As shown in Figure 5, the first step involved excluding catalysts with poor stability and weak N_2 adsorption capacity. As a result, 99 candidate catalysts were screened from 171 species, all of which exhibited good stability and high N_2 adsorption. In the second step, the 99 catalysts were further screened for activity, and it was found that only 4 out of the 99 catalysts met the set conditions and could achieve a low reaction energy pathway. Ultimately, we identified four highly active candidate catalysts: Ti-Mo@N_6G, Ti-Cr@N6G, Ti-Pd@N_6G, and Ti-Co@N_6G.

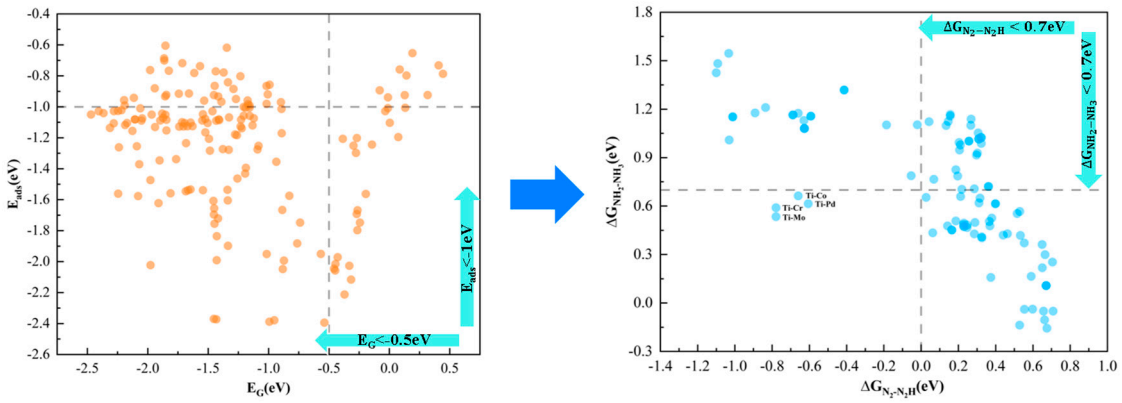


Figure 5. ML screened 171 TM_1-TM_2@N_6G catalysts.

2.3. Performance Exploration of TM_1-TM_2@N6G Candidates

To further investigate the catalytic performance of the four screened TM_1-TM_2@N_6G catalysts, AIMD simulations were conducted at 500 K and 600 K, respectively, to evaluate their stability using 1 fs time steps over a total simulation time of 10 ps. As shown in Figure 6a–d, the energy and structure of the four TM_1-TM_2@N_6G catalysts remained stable at high temperatures of 500 K and 600 K, with the two TM atoms firmly bound to the six N atoms on the catalyst without any significant structural distortion. This demonstrates that the four TM_1-TM_2@N_6G catalysts exhibit thermal stability and are capable of withstanding high temperatures.

To assess the activation mechanism and explore N_2 adsorption on the four catalysts, the presence of two active sites in the bimetallic atom catalyst introduced diversity in N_2 adsorption, revealing new activation possibilities and reaction pathways. As evident from Figure S1, there are three forms of N_2 adsorption on the catalyst surface: single adsorption structure, bridge adsorption structure, and parallel adsorption structure. Detailed information, including the calculated adsorption energy (E_{ads}), the length of the N≡N bond under different adsorption structures, and the Bader charge, is presented in Table 3. The adsorption energy is linearly related to the adsorption strength, with a more negative adsorption energy indicating a stronger adsorption intensity of the corresponding adsorbate. According to Table 3, the N_2 adsorption energies for Ti-Co-Parallel, Ti-Co-Single, Ti-Mo-Parallel, Ti-Cr-Parallel, and Ti-Pd-Single were −0.733, −0.748, −2.014, −2.020, and −1.134 eV, respectively. It was observed that the four candidate catalysts did not exhibit a bridge adsorption structure, and the single adsorption structure and parallel adsorption structure demonstrated a stronger preference for N_2 adsorption. Among these, Ti-Mo-Parallel and Ti-Cr-Parallel showed a particularly strong adsorption trend.

Table 3. Stable adsorption structure details of candidate catalysts.

	N≡N/Å			Bader/e$^-$			Eads/eV		
	Bridge	**Parallel**	**Single**	**Bridge**	**Parallel**	**Single**	**Bridge**	**Parallel**	**Single**
Ti-Co	—	1.214	1.145	—	−0.690	−0.363	—	−0.733	−0.748
Ti-Mo	—	1.245	—	—	−1.008	—	—	−2.014	—
Ti-Cr	—	1.249	—	—	−0.926	—	—	−2.020	—
Ti-Pd	—	—	−1.138	—	—	−0.279	—	—	−1.134

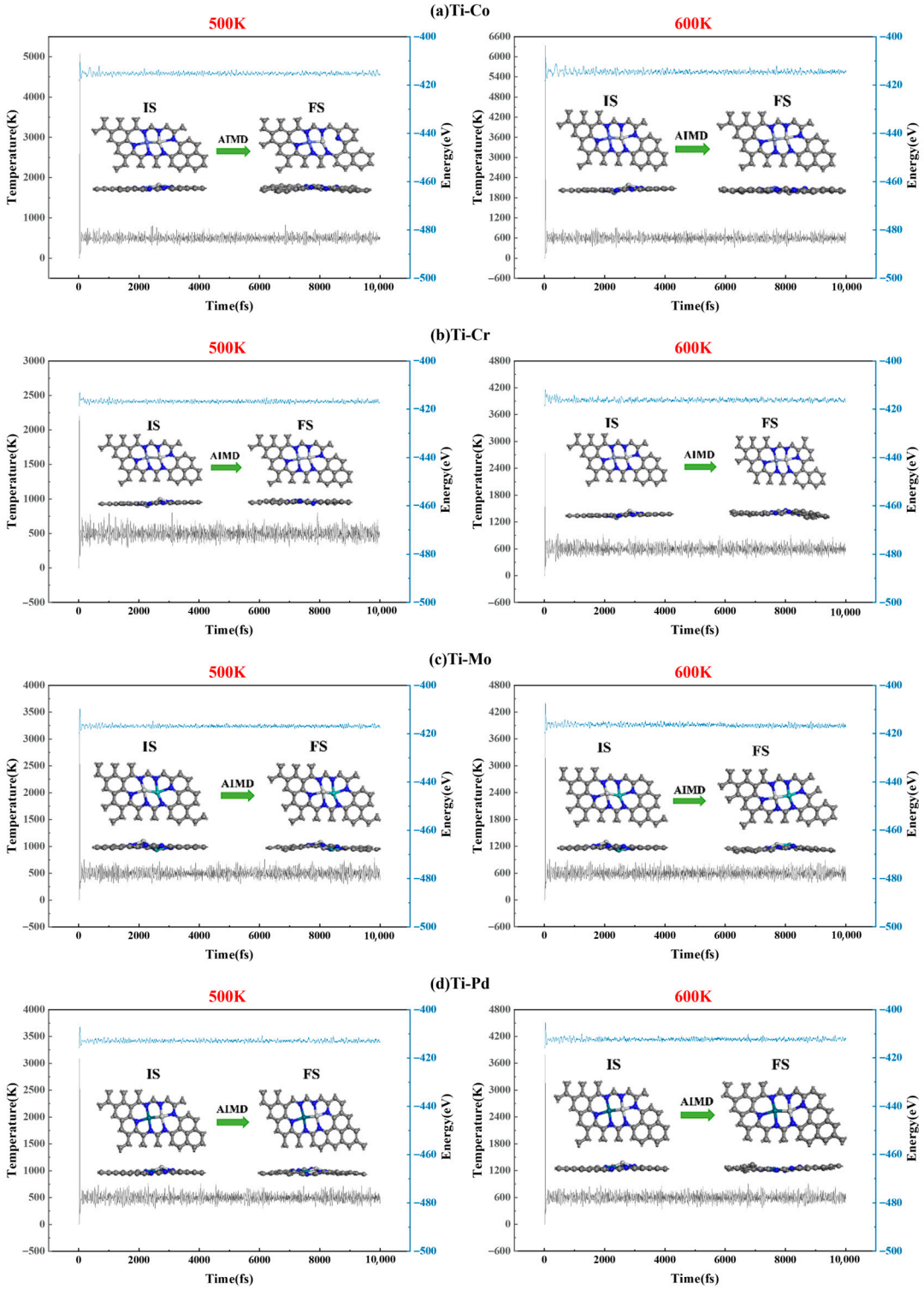


Figure 6. Changes in energy and temperature during AIMD simulation of (**a**) Ti-Co, (**b**) Ti-Cr, (**c**) Ti-Mo, and (**d**) Ti-Pd.

The activation mechanism of N_2 by the four candidate catalysts was further revealed, and the differential charge density map of the adsorption structure was obtained. As shown in Figure 7, the cyan area represents charge loss, and the yellow area represents charge accumulation. According to the differential charge density diagram, there is a large amount of electron transfer between the active site and N_2 when N_2 is adsorbed on the surface. Significant charge loss occurs at the N≡N bond, which weakens the N≡N interaction and realizes the activation of N_2. It can be seen that the parallel adsorption structure has more

advantages in activating N_2 molecules, and the Ti-Mo-Parallel and Ti-Cr-Parallel surfaces obtain charges of 1.008 and 0.926e$^-$, which are more dense than those of the single adsorption structure, indicating that the parallel adsorption structure is more conducive to the transfer of charge from the catalyst to the adsorbate. The corresponding N≡N bond length (between 1.145 Å and 1.249 Å) varies with the number of transferred electrons. The increase in N≡N bond length after adsorption further confirmed the effective activation of N_2.

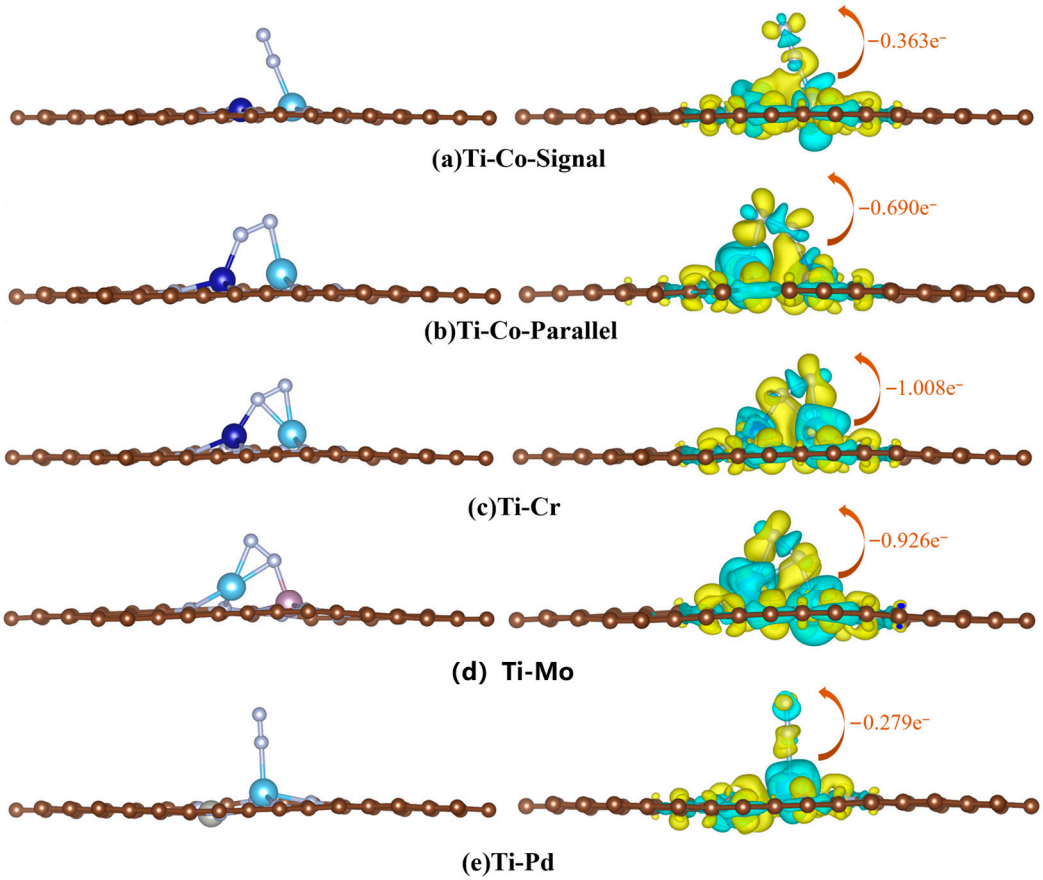


Figure 7. Diagram of the adsorption structure and the corresponding differential charge density of the candidate DACs.

To reveal the microscopic electron distribution and density of states of the catalyst, projected density of states (PDOS) calculations and energy band diagrams of the catalyst were performed, with the Fermi level set to 0. As shown in Figure 8, there is evident hybridization and coupling between the p orbital of the N_2 molecule and the d orbital of the active site in the catalyst. The significant overlap of the d and p orbitals indicates a strong bond between the N_2 molecules and the substrate, which is advantageous for the capture of N_2. The interaction between N_2 and TM_1-TM_2@N_6G follows the well-established donation–back-donation mechanism. Specifically, electrons from the filled π orbitals of N_2 are donated to the unoccupied d orbitals of the TM metal atom, while the occupied d orbitals of the TM atom back-donate electrons into the antibonding π* orbitals of N_2. This synergistic donation and back-donation interaction facilitates the activation of the N≡N bond, confirming that the four catalysts exhibit strong adsorption and high activity towards N_2.

As illustrated in Figure 9a–d, the four catalysts, namely Ti-Co@N_6G, Ti-Cr@N_6G, Ti-Mo@N_6G, and Ti-Pd@N_6G, all exhibit narrow band gaps. Among them, Ti-Pd@N_6G has the narrowest spin-down band gap of 0.0018 eV, while Ti-Mo@N_6G displays the narrowest spin-up band gap of 0.0024 eV. A narrower band gap signifies a higher electron transfer

and transmission rate on the catalyst surface, resulting in faster internal electron transitions and, consequently, enhanced catalyst activity.

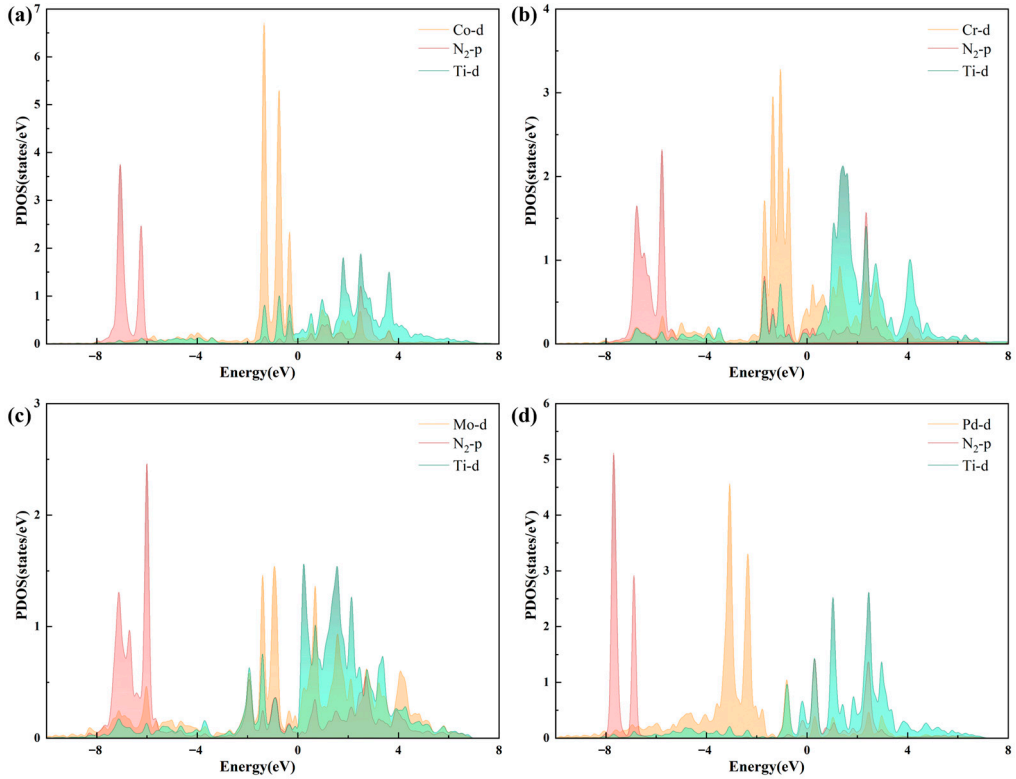


Figure 8. The projected density of states (PDOS) of (**a**) Ti-Co, (**b**) Ti-Cr, (**c**) Ti-Mo, and (**d**) Ti-Pd.

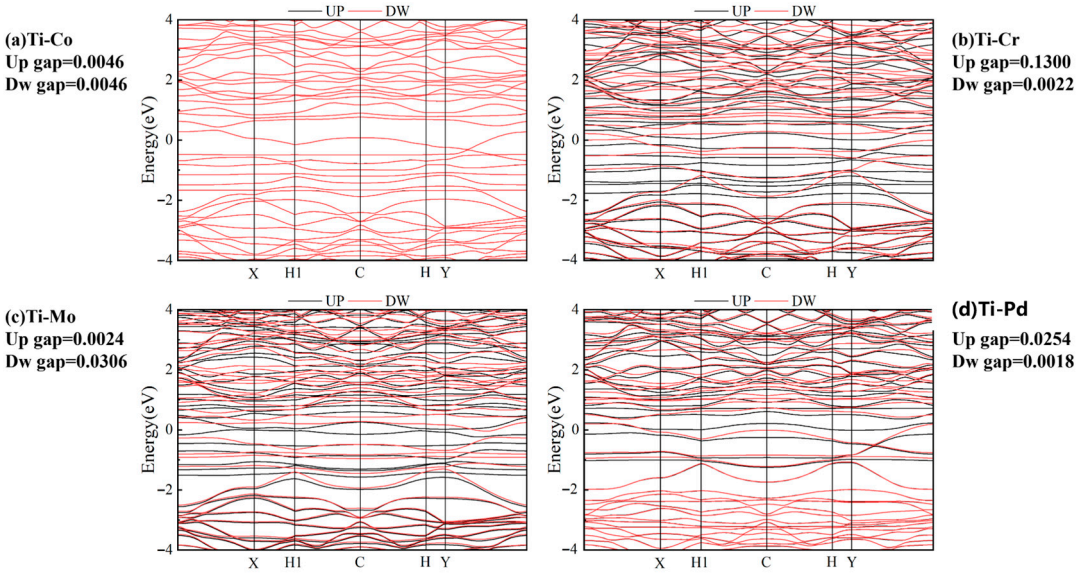


Figure 9. Band structure of (**a**) Ti-Co, (**b**) Ti-Cr, (**c**) Ti-Mo, and (**d**) Ti-Pd. Spin-up band gap and spin-down band gap are labeled separately.

To comprehensively assess the activity of the catalyst and verify its validity and accuracy, a detailed exploration of the NRR mechanism was conducted for the four catalyst structures. During the screening process, only intermediates with stable structures were retained. The NRR mechanism diagram and the corresponding intermediate structure diagrams are presented in Figure 10a–d. All four catalysts demonstrate excellent catalytic performance. Specifically, Ti-Co@N_6G exhibits only one favorable NRR pathway. In

contrast, Ti-Cr@N_6G, Ti-Mo@N_6G, and Ti-Pd@N_6G possess two favorable pathways, which can be categorized as the far-end and alternating paths:

$$*N_2 \rightarrow *NNH \rightarrow *NNH_2 \rightarrow *N \rightarrow *NH \rightarrow *NH_2 \rightarrow *NH_2{+}1/2H_2 \rightarrow NH_3(g)$$

$$*N_2 \rightarrow *NNH \rightarrow *NHNH \rightarrow *NHNH_2 \rightarrow *NH_2 \rightarrow *NH \rightarrow *NH_2 \rightarrow *NH_2{+}1/2H_2 \rightarrow NH_3(g).$$

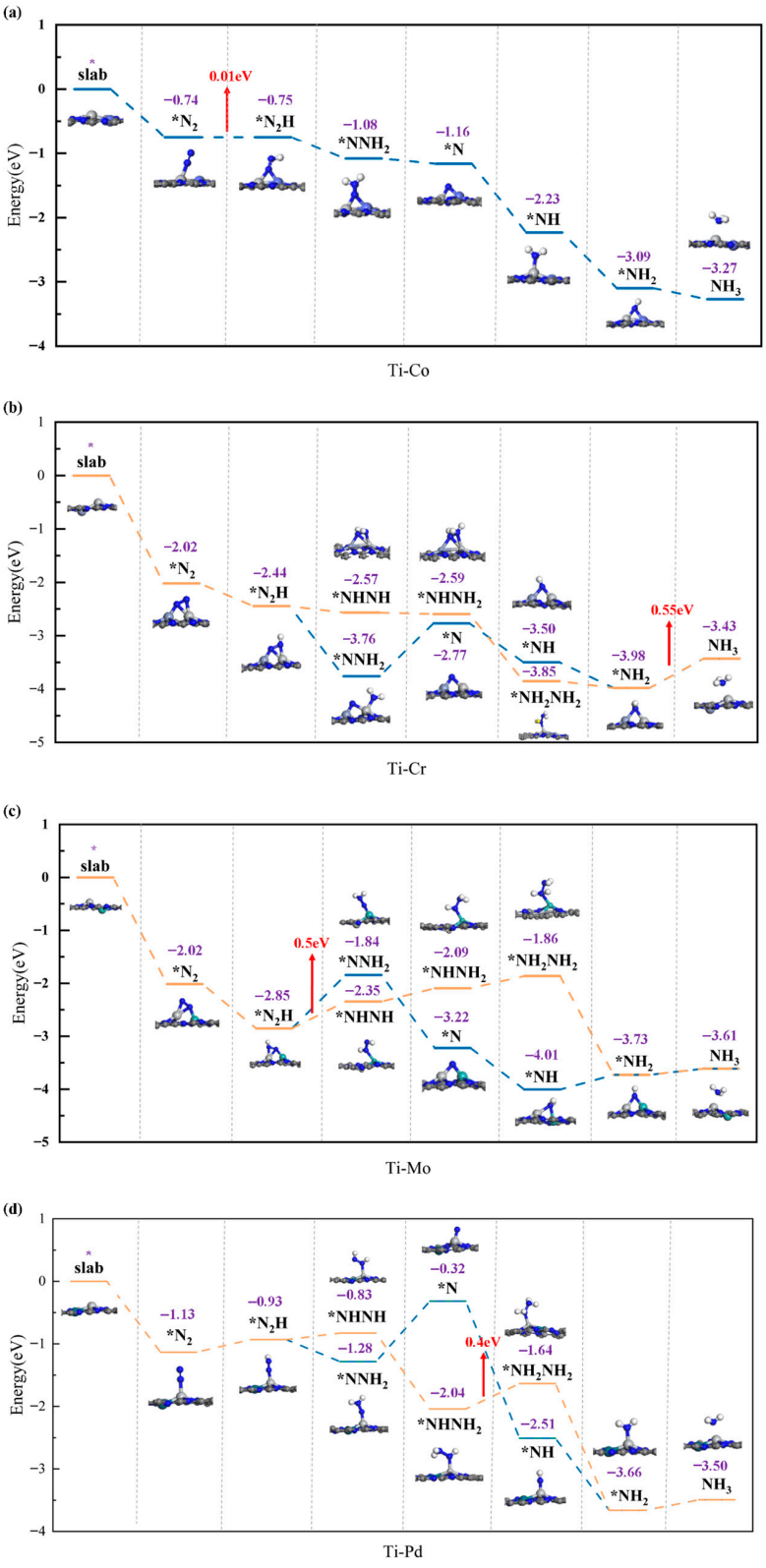


Figure 10. (**a**) Ti-Co, (**b**) Ti-Cr, (**c**) Ti-Mo, and (**d**) Ti-Pd free energy distribution and reaction energy (* The symbol is used to indicate the intermediates adsorbed on the surface of the catalyst).

From Figure 10b–d, it can be seen that the reaction energies of the alternating paths in Ti-Cr@N_6G, Ti-Mo@N_6G, and Ti-Pd@N_6G are much smaller than those of the distal paths, and the reaction energies are 0.55 eV, 0.5 eV, and 0.4 eV, respectively. There is only a distal path in the Ti-Co@N_6G catalyst, and the best NRR path reaction energy is 0.01 eV, which can realize the spontaneous catalysis of the NRR process. In addition, it is worth noting that it can be observed from Figure 10a–d that the first hydrogenation reaction of nitrogen can occur without or with very little external energy input, which is not common in previous related studies. This phenomenon further reveals that the adsorbed N_2 molecules are highly activated by the catalyst, and the interaction between N≡N bonds is greatly reduced, which further improves the catalytic efficiency.

3. Computational Details

The density functional theory (DFT) calculations in this study were performed using the Vienna Ab initio Simulation Package (VASP) [42]. The interaction between electrons and ions was described using the Projector Augmented Wave (PAW) method. The exchange correlation was described by the Generalized Gradient Approximation (GGA) in the Perdew–Burke–Ernzerhof (PBE) parameterization [43]. The weak van der Waals interaction between the substrate and the adsorbate was corrected using the DFT-D_3 method [44]. The cut-off energy was set to 400 eV. A vacuum layer of 15 Å was established to prevent periodic repetitive effects during structural relaxation. The transition metal diatomic catalyst model was created by doping six nitrogen atoms onto a $4 \times 4 \times 1$ graphene supercell and anchoring the transition metal atom pair. The first Brillouin zone was sampled using the Monkhorst–Pack method, with the Kpoints file set to $3 \times 4 \times 1$. The energy convergence criterion was set to 1×10^{-6} eV. The charge transfer and distribution between the intermediate and the substrate were quantified using Bader charge analysis [45].

The thermodynamic stability of TM_1-TM_2@N_6G was investigated through AIMD calculations at 600 K, with a 10 ps simulation duration and 1 fs time steps. The data generated by VASP were analyzed using VASPKIT [46]. The s, d orbital projected density of states (PDOS) of the active center metal atoms and the p orbital PDOS of the N_2 small molecule were calculated and plotted to describe the electron distribution within each orbital. These charts were used to analyze atom-to-atom interactions and provide insights into the details of chemical bonds. To ensure the accuracy of the results, a NEDOS value of 4000 was employed in this study.

To demonstrate the feasibility and stability of the diatomic catalyst, the binding energies (E_G) of TM_1-TM_2@N_6G were calculated:

$$E_G = E_{slab} - E_{N-graphite} - \mu_M - \mu_X, \quad (1)$$

E_{slab} and $E_{N-graphite}$ are the total energies of TM_1-TM_2@N_6G and N-doped graphite, respectively. μ_M and μ_X represent the chemical potential of each metal element, respectively.

To evaluate the stability of TM_1-TM_2@N_6G adsorption to N_2, the adsorption energies (E_{ads}) of NRR intermediates were calculated.

$$E_{ads} = E_{total} - E_{Rel} - E_{sub} \quad (2)$$

E_{sub} and E_{Rel} represent the energy of the substrate and the relaxed adsorbate, respectively. The energy of the adsorption system is denoted by E_{total}. The larger the absolute value of the adsorption energy (E_{ads}), the more stable the adsorption structure is.

To study the reaction mechanism of N_2 and H_2 converting to NH_3 in TM_1-TM_2@N_6G diatomic catalysts, the change in the intermediate reaction energy at each step, denoted as ΔG, was calculated.

$$\Delta G = E_{aft} - E_{bef} - E_{ecp}, \quad (3)$$

ΔG denotes the energy difference of the intermediate before and after the reaction. E_{bef} and E_{aft} represent the energy of the intermediate before and after the reaction, and E_{ecp} represents the energy change in the elements involved in the reaction. This value does not represent a true activation energy derived from a transition state calculation but rather serves as an effective descriptor to assess catalytic trends.

Three different supervised machine learning algorithms were utilized in the machine learning process: the random forest algorithm (RFR) [47], k-nearest neighbor regression (KNR) [48], and decision tree (DT) [49]. These algorithms were implemented in the Python3 environment using the open-source Scikit-learn and PyTorch packages [50]. The input data, generated by DFT computations and the database, was trained and divided into a training set and a test set at a ratio of 8:2. All data was normalized during both training and prediction. The performance of each ML model was evaluated using two indicators: root mean square error (RMSE) and the coefficient of determination (R^2), which are expressed as follows:

$$\mathrm{RMSE} = \sqrt{\frac{1}{n}\sum_{i=1}^{n}(p_i - y_i)^2} \tag{4}$$

$$R^2 = 1 - \frac{\sum_{i=1}^{n}(p_i - y_i)^2}{\sum_{i=1}^{n}(p_i - \overline{y_i})^2} \tag{5}$$

where y_i represents the true value and p_i represents the model's predicted value. For an accurate model, the RMSE should ideally be as close to 0 as possible, and the R^2 score should be as close to 1 as possible.

4. Summary and Conclusions

In summary, in this study, the performance of 171 different DACs catalyzed by 17 transition metal elements in pairs was systematically investigated by combining DFT computation and machine learning methods. In this study, 25 randomly selected DACs were calculated by DFT to obtain key intermediates and their free energy changes, and combined with the physical parameters of the corresponding metal atoms constituting DACs, they were used as the training set for machine learning research for effective model training. It was found that the model based on the RFR algorithm had the highest prediction accuracy for the adsorption energy of reaction intermediates ($R^2 > 0.9$, RMSE < 0.18). Based on the constraints of catalyst binding energy, nitrogen adsorption energy, the first hydrogenation step, and ammonia dissociation, four candidate high-activity catalysts were screened out. Through performance exploration, it is found that the synergistic effect of the TM_1-TM_2@N_6G catalyst and two TM atoms breaks the inherent limitation of the linear relationship between intermediates, promotes the activation and adsorption of N_2, and has great potential for the deep reduction of N_2. The four candidate catalysts screened showed excellent stability, significant affinity, and high selectivity for N_2. Among them, Ti-Cr@N_6G, Ti-Mo@N_6G, and Ti-Pd@N_6G catalysts have two different reaction paths, and the lowest reaction energies appear on the alternating path, which are 0.55 eV, 0.5 eV, and 0.4 eV, respectively. The reaction of Ti-Co@N_6G only follows the distal path, and its reaction energy is extremely low, only 0.01 eV, which means that Ti-Co@N_6G can spontaneously catalyze during the NRR process. The method proposed in this paper to determine the performance of catalysts by descriptors by combining ML and DFT greatly reduces the cost of calculation and can quickly and accurately determine the highly active candidate catalysts in a class of catalysts, thus providing a new perspective for the design of NRR catalysts with excellent catalytic performance.

Supplementary Materials: The following supporting information can be downloaded at https://www.mdpi.com/article/10.3390/molecules30204131/s1, Table S1: Contains four descriptor pa-

rameters. Figure S1: Schematic diagram of common adsorption structures of NRR. Figure S2: Comparision between DFT calculation results and RFR predictions for (a) ΔE_G, (b) E_{ads}, (c) $\Delta G_{N_2-N_2H}$, (d) $\Delta G_{NH_2-NH_3}$.

Author Contributions: Conceptualization, H.Y.; methodology, X.W. (Xiulin Wang) and Y.L.; software, Y.L. and J.F.; validation, S.W. and Y.S.; investigation, Y.L.; data curation, Y.L. and J.F.; writing—original draft preparation, Y.L.; writing—review and editing, Y.L. and J.F.; visualization, Y.Z.; supervision, X.W. (Xinwei Wang); project administration, S.N.; funding acquisition, X.Z. All authors have read and agreed to the published version of the manuscript.

Funding: This research was supported by the Open Fund Project of CNOOC Key Laboratory of Liquefied Natural Gas and Low-carbon Technology (QDKJZH-2024-65).

Institutional Review Board Statement: Not applicable.

Informed Consent Statement: Not applicable.

Data Availability Statement: Data will be made available on request.

Conflicts of Interest: Authors Xiulin Wang, Suofu Nie, Huichao Yao, Sida Wu, Yiyan Sui, Yuqing Zhang were employed by the company CNOOC. The remaining authors declare that the research was conducted in the absence of any commercial or financial relationships that could be construed as a potential conflict of interest. The authors declare that this study received funding from CNOOC. The funder was not involved in the study design, collection, analysis, interpretation of data, the writing of this article or the decision to submit it for publication.

Abbreviations

The following abbreviations are used in this manuscript:

NRR	Nitrogen reduction reaction
ML	Machine learning
DFT	Density functional theory
SACs	Single-atom catalysts
DACs	Dual-atom catalysts
N_6G	6-nitrogen-doped graphene
AIMD	Ab initio molecular dynamics
PDOS	Projected density of states
VASP	Vienna Ab initio Simulation Package
PAW	Projector Augmented Wave
GGA	Generalized Gradient Approximation
PBE	Perdew–Burke–Ernzerhof
RFR	Random Forest Algorithm
KNN	K-nearest Neighbor Regression
DT	Decision Tree
RMSE	Root mean square error
R^2	Coefficient of determination

References

1. Klerke, A.; Christensen, C.H.; Nørskov, J.K.; Vegge, T. Ammonia for hydrogen storage: Challenges and opportunities. *J. Mater. Chem.* **2008**, *18*, 2304–2310. [CrossRef]
2. Schlögl, R. Catalytic synthesis of ammonia—A "never-ending story"? *Angew. Chem. Int. Ed.* **2003**, *42*, 2004–2008. [CrossRef]
3. Smil, V. Detonator of the population explosion. *Nature* **1999**, *400*, 415. [CrossRef]
4. Chen, X.; Li, N.; Kong, Z.; Ong, W.; Zhao, X. Photocatalytic fixation of nitrogen to ammonia: State-of-the-art advancements and future prospects. *Mater. Horiz.* **2018**, *5*, 9–27. [CrossRef]
5. Saadatjou, N.; Jafari, A.; Sahebdelfar, S. Ruthenium nanocatalysts for ammonia synthesis: A review. *Chem. Eng. Commun.* **2015**, *202*, 420–448. [CrossRef]

6. Qiao, B.; Wang, A.; Yang, X.; Allard, L.; Jiang, Z.; Cui, Y.; Liu, J.; Li, J.; Zhang, T. Single-atom catalysis of CO oxidation using Pt_1/FeO_x. *Nat. Chem.* **2011**, *3*, 634–641. [CrossRef]
7. Shi, M.M.; Bao, D.; Li, S.J.; Wulan, B.; Jiang, Q. Anchoring Pd-Cu amorphous nanocluster on graphene for electrochemical reduction of N_2 to NH_3 under ambient conditions in aqueous solution. *Adv. Energy Mater.* **2018**, *8*, 1800124. [CrossRef]
8. Shi, M.M.; Bao, D.; Wulan, B.R.; Li, Y.H.; Zhang, Y.F.; Yan, J.M.; Jiang, Q. Au sub-nanoclusters on TiO_2 toward highly efficient and selective electro catalyst for N_2 conversion to NH_3 at ambient conditions. *Adv. Mater.* **2017**, *29*, 1606550. [CrossRef]
9. Chen, Y.; Ji, S.; Chen, C.; Peng, Q.; Wang, D. Single-atom catalysts: Synthetic strategies and electrochemical applications. *Joule* **2018**, *2*, 1242–1264. [CrossRef]
10. Zhu, C.; Fu, S.; Shi, Q.; Du, D.; Lin, Y. Single-atom electro catalysts. *Angew. Chem. Int. Ed.* **2017**, *56*, 13944–13960. [CrossRef]
11. Li, X.F.; Li, Q.K.; Cheng, J.; Liu, L.L.; Yan, Q.; Wu, Y.C.; Zhang, X.H.; Wang, Z.Y.; Qi, Q.; Luo, Y. Conversion of dinitrogen to ammonia by FeN_3-embedded graphene. *J. Am. Chem. Soc.* **2016**, *138*, 8706–8709. [CrossRef] [PubMed]
12. Deng, J.; Li, H.; Xiao, J.; Tu, Y. Triggering the electro catalytic hydrogen evolution activity of the inert two-dimensional MoS_2 surface via single-atom metal doping. *Energy Environ. Sci.* **2015**, *8*, 1594–1601. [CrossRef]
13. Wang, Y.; Arandiyan, H.; Scott, J.; Auguey-Zinsou, K.; Amal, R. Single atom and nanocluster Pt catalysts for selective CO_2 reduction. *ACS Appl. Energy Mater.* **2018**, *1*, 6781–6789. [CrossRef]
14. Wang, S.; Yu, W.; Xu, S.; Han, K.; Wang, F. Ammonia from photothermal N_2 hydrogenation over Ni/TiO_2 catalysts under mild conditions. *ACS Sustain. Chem. Eng.* **2021**, *10*, 115–123. [CrossRef]
15. Cao, X.; Xing, S.; Ma, D.; Tan, Y.; Zhu, Y.; Hu, J. Design of high-performance ion-doped Co-P systems for hydrogen evolution: From multi-level screening calculations to experiment. *J. Energy Chem.* **2023**, *82*, 307–316. [CrossRef]
16. Wan, X.; Zhang, Z.; Niu, H.; Yin, Y.; Kuai, C.; Wang, J.; Shao, C.; Guo, Y. Machine-learning-accelerated catalytic activity predictions of transition metal phthalocyanine dual-metal-site catalysts for CO_2 reduction. *J. Phys. Chem. Lett.* **2021**, *12*, 6111–6118. [CrossRef]
17. Sun, M.; Dougherty, A.W.; Huang, B.; Li, Y.; Yan, C. Accelerating atomic catalyst discovery by theoretical calculations-machine learning strategy. *Adv. Energy Mater.* **2020**, *10*, 1903949. [CrossRef]
18. Zafari, M.; Kumar, D.; Umer, M.; Kim, K. Machine learning-based high throughput screening for nitrogen fixation on boron-doped single atom catalysts. *J. Mater. Chem. A* **2020**, *8*, 5209–5216. [CrossRef]
19. Van Santen, R.A. Complementary structure sensitive and insensitive catalytic relationships. *Acc. Chem. Res.* **2009**, *42*, 57–66. [CrossRef]
20. Li, Z.; Wang, S.; Xin, H. Toward artificial intelligence in catalysis. *Nat. Catal.* **2018**, *1*, 641–642. [CrossRef]
21. Ma, S.; Liu, Z.P. Machine learning for atomic simulation and activity prediction in heterogeneous catalysis: Current status and future. *ACS Catal.* **2020**, *10*, 13213–13226. [CrossRef]
22. Chen, L.; Zhang, X.; Chen, A.; Yan, S.; Hu, X.; Zhou, Z. Targeted design of advanced electrocatalysts by machine learning. *Chin. J. Catal.* **2022**, *43*, 11–32. [CrossRef]
23. Liu, J.; Luo, W.; Wang, L.; Zhang, J.; Fu, X.; Luo, J. Toward excellence of electrocatalyst design by emerging descriptor-oriented machine learning. *Adv. Funct. Mater.* **2022**, *32*, 2110748. [CrossRef]
24. Tabor, D.P.; Roch, L.M.; Saikin, S.K.; Kreisbeck, C.; Sheberla, D.; Montoya, J.; Dwaraknath, S.; Aykol, M.; Ortiz, C.; Tribukait, H.; et al. Accelerating the discovery of materials for clean energy in the era of smart automation. *Nat. Rev. Mater.* **2018**, *3*, 5–20. [CrossRef]
25. Tran, K.; Ulissi, Z.W. Active learning across intermetallics to guide discovery of electrocatalysts for CO_2 reduction and H_2 evolution. *Nat. Catal.* **2018**, *1*, 696–703. [CrossRef]
26. Zhong, M.; Tran, K.; Min, Y.; Wang, C.; Wang, Z.; Dinh, C.; Luna, P.; Yu, Z.; Rasouli, A.; Brodersen, P.; et al. Accelerated discovery of CO_2 electrocatalysts using active machine learning. *Nature* **2020**, *581*, 178–183. [CrossRef]
27. O'Connor, N.J.; Jonayat, A.S.M.; Janik, M.J.; Senftle, T. Interaction trends between single metal atoms and oxide supports identified with density functional theory and statistical learning. *Nat. Catal.* **2018**, *1*, 531–539. [CrossRef]
28. Panapitiya, G.; Avendaño-Franco, G.; Ren, P.; Wen, X.; Li, Y.; Lewis, J.P. Machine-learning prediction of CO adsorption in thiolated, Ag-alloyed Au nanoclusters. *J. Am. Chem. Soc.* **2018**, *140*, 17508–17514. [CrossRef]
29. Wexler, R.B.; Martirez, J.M.P.; Rappe, A.M. Chemical pressure-driven enhancement of the hydrogen evolving activity of Ni_2P from nonmetal surface doping interpreted via machine learning. *J. Am. Chem. Soc.* **2018**, *140*, 4678–4683. [CrossRef]
30. Wu, L.; Guo, T.; Li, T. Rational design of transition metal single-atom electrocatalysts: A simulation-based, machine learning-accelerated study. *J. Mater. Chem. A* **2020**, *8*, 19290–19299. [CrossRef]
31. Ma, X.; Li, Z.; Achenie, L.E.K.; Xin, H. Machine-learning-augmented chemisorption model for CO_2 electroreduction catalyst screening. *J. Phys. Chem. Lett.* **2015**, *6*, 3528–3533. [PubMed]
32. Boonpalit, K.; Wongnongwa, Y.; Prommin, C.; Nutanong, S.; Numuangruk, S. Data-driven discovery of graphene-based dual-atom catalysts for hydrogen evolution reaction with graph neural network and DFT calculations. *ACS Appl. Mater. Interfaces* **2023**, *15*, 12936–12945.

33. Wang, S.; Qian, C.; Zhou, S. Machine learning design of single-atom catalysts for nitrogen fixation. *ACS Appl. Mater. Interfaces* **2023**, *15*, 40656–40664. [CrossRef] [PubMed]
34. Kumar, A.; Sun, K.; Duan, X.; Tian, S.; Sun, X. Construction of dual-atom Fe via face-to-face assembly of molecular phthalocyanine for superior oxygen reduction reaction. *Chem. Mater.* **2022**, *34*, 5598–5606. [CrossRef]
35. Wang, J.; Liu, W.; Luo, G.; Li, Z.; Zhao, C.; Zhang, H.; Zhu, M.; Xu, Q.; Wang, X.; Zhao, C.; et al. Synergistic effect of well-defined dual sites boosting the oxygen reduction reaction. *Energy Environ. Sci.* **2018**, *11*, 3375–3379. [CrossRef]
36. Liu, X.; Qi, L.; Song, E.; Gao, W. Effective descriptor for nitrogen reduction on atomic catalysts. *Catal. Lett.* **2023**, *153*, 300–310.
37. Hu, X.; Su, N.Q.; Fang, W.H. Metallated graphynes as efficient single-atom electrocatalysts for nitric oxide reduction to ammonia. *J. Phys. Chem. C* **2023**, *127*, 11026–11039. [CrossRef]
38. Zhao, Z.; Hu, M.; Nie, T.; Zhou, W.; Pan, B.; Xing, B.; Zhu, L. Improved electronic structure from spin-state reconstruction of a heteronuclear Fe-Co diatomic pair to boost the Fenton-like reaction. *Environ. Sci. Technol.* **2023**, *57*, 4556–4567. [CrossRef]
39. Ling, C.; Ouyang, Y.; Li, Q.; Bai, X.; Mao, X.; Du, A.; Wang, J. A general two-step strategy–based high-throughput screening of single atom catalysts for nitrogen fixation. *Small Methods* **2019**, *3*, 1800376. [CrossRef]
40. Seh, Z.W.; Kibsgaard, J.; Dickens, C.F.; Chorkendorff, I.; Nørskov, J.S.; Jaramillo, T.F. Combining theory and experiment in electrocatalysis: Insights into materials design. *Science* **2017**, *355*, eaad4998. [CrossRef]
41. Skulason, E.; Bligaard, T.; Gudmundsdóttir, S.; Studt, F.; Rossmeisl, J.; Abild-Pedersen, F.; Vegge, T.; Jónsson, H.; Nørskov, J. A theoretical evaluation of possible transition metal electro-catalysts for N_2 reduction. *Phys. Chem. Chem. Phys.* **2012**, *14*, 1235–1245. [CrossRef]
42. Kresse, G.; Furthmuller, J. Efficient iterative schemes for ab initio total-energy calculations using a plane-wave basis set. *Phys. Rev. B* **1996**, *54*, 11169. [CrossRef]
43. Perdew, J.P.; Burke, K.; Ernzerhof, M. Generalized gradient approximation made simple. *Phys. Rev. Lett.* **1996**, *77*, 3865. [CrossRef] [PubMed]
44. Grimme, S.; Antony, J.; Ehrlich, S.; Krieg, H. A consistent and accurate ab initio parametrization of density functional dispersion correction (DFT-D) for the 94 elements H-Pu. *J. Chem. Phys.* **2010**, *132*, 154104. [CrossRef] [PubMed]
45. Henkelman, G.; Arnaldsson, A.; Jónsson, H. A fast and robust algorithm for Bader decomposition of charge density. *Comput. Mater. Sci.* **2006**, *36*, 354–360. [CrossRef]
46. Wang, V.; Xu, N.; Liu, J.C.; Tang, G.; Geng, W. VASPKIT: A user-friendly interface facilitating high-throughput computing and analysis using VASP code. *Comput. Phys. Commun.* **2021**, *267*, 108033. [CrossRef]
47. Liaw, A.; Wiener, M. Classification and regression by randomForest. *R News* **2002**, *2*, 18–22.
48. Devroye, L.; Gyorfi, L.; Krzyzak, A.; Lugosi, G. On the strong universal consistency of nearest neighbor regression function estimates. *Ann. Stat.* **1994**, *22*, 1371–1385. [CrossRef]
49. Aksöz, Z.Y.; Günay, M.E.; Aziz, M.; Tunc, K. Machine Learning Analysis of Thermal Performance Indicator of Heat Exchangers with Delta Wing Vortex Generators. *Energies* **2024**, *17*, 1380. [CrossRef]
50. Pedregosa, F. Scikit-learn: Machine learning in python Fabian. *J. Mach. Learn. Res.* **2011**, *12*, 2825.

Disclaimer/Publisher's Note: The statements, opinions and data contained in all publications are solely those of the individual author(s) and contributor(s) and not of MDPI and/or the editor(s). MDPI and/or the editor(s) disclaim responsibility for any injury to people or property resulting from any ideas, methods, instructions or products referred to in the content.